UC San Diego
UC San Diego Previously Published Works

Title
Identifying the chemical and structural irreversibility in LiNi 0.8 Co 0.15 Al 0.05 O 2 – a model compound for classical layered intercalation

Permalink
https://escholarship.org/uc/item/3s9491vc

Journal
Journal of Materials Chemistry A, 6(9)

ISSN
2050-7488

Authors
Liu, Haodong
Liu, Hao
Seymour, Ieuan D
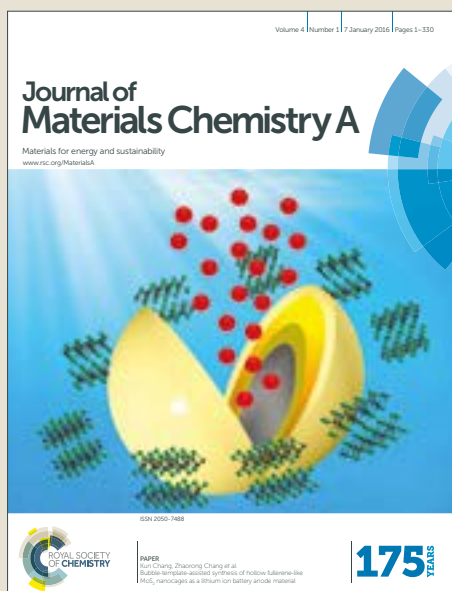et al.

Publication Date
2018

DOI
10.1039/c7ta10829j

Peer reviewed

Journal of
Materials Chemistry A

Accepted Manuscript

Volume 4 | Number 1 | 7 January 2016 | Pages 1–330

Journal of
Materials Chemistry A

Materials for energy and sustainability
www.rsc.org/MaterialsA

ISSN 2050-7488

ROYAL SOCIETY OF CHEMISTRY

PAPER
Kun Chang, Zhaorong Chang et al.
Bubble-template-assisted synthesis of hollow fullerene-like
MoS₂ nanocages as a lithium ion battery anode material

175 YEARS

This is an Accepted Manuscript, which has been through the Royal Society of Chemistry peer review process and has been accepted for publication.

Accepted Manuscripts are published online shortly after acceptance, before technical editing, formatting and proof reading. Using this free service, authors can make their results available to the community, in citable form, before we publish the edited article. We will replace this Accepted Manuscript with the edited and formatted Advance Article as soon as it is available.

You can find more information about Accepted Manuscripts in the author guidelines.

ROYAL SOCIETY OF CHEMISTRY

rsc.li/materials-a

ARTICLE

Identifying the chemical and structural irreversibility in LiNi$_{0.8}$Co$_{0.15}$Al$_{0.05}$O$_2$ - A model compound for classical layered intercalation

Haodong Liu[a], Hao Liu[b], Ieuan D. Seymour[c], Natasha Chernova[d], Kamila M. Wiaderek[b], Nicole M. Trease[c], Sunny Hy[a], Yan Chen[e], Ke An[e], Minghao Zhang[a], Olaf J. Borkiewicz[b], Saul H. Lapidus[b], Bao Qiu[f], Yonggao Xia[f], Zhaoping Liu[f], Peter J. Chupas[b], Karena W Chapman[b], M. Stanley Whittingham[d], Clare P. Grey[c], Ying Shirley Meng[a]*

In this work, we extracted 95% of the electrochemically available Li from LiNi$_{0.8}$Co$_{0.15}$Al$_{0.05}$O$_2$ (NCA) by galvanostatically charging the NCA/MCMB full cell to 4.7V. Joint powder X-ray and neutron diffraction (XRD&ND) studies were undertaken for NCA at highly charged states at the first cycle, and discharged states at different cycles. The results indicate that the bulk structure of NCA maintains the O3 structure up to the extraction of 0.90 Li per formula unit. In addition, we found that the transition metal layer becomes more disordered along the c-axis than along the a- and b- axes upon charging. This anisotropic disorder starts to develop no later than 4.3 V on charge and continues to grow until the end of charge. As Li is re-inserted during discharge, the structure that resembles the pristine NCA is recovered. The irreversible loss of Li and the migration of Ni to the Li layer have been quantified by the joint XRD and ND refinement and the results were further verified by solid state ^{7}Li NMR and magnetic measurements. Our work clearly demonstrates that the NCA bulk retains a robust, single phase O3 structure throughout the wide delithiation range (up to 0.9 Li per formula unit of NCA) and is suitable for higher energy density usage with proper modifications.

Introduction

In 2012, Tesla launched Model S, a premium pure electric vehicle. After a short period of three years and six months, Tesla sold its 100,000th Model S in December 2015[1]. This electric car has achieved a long driving range of 265 miles (426 km) per charge, which is close to the range of traditional gasoline vehicles.[2] The lithium nickel cobalt aluminum oxide (LiNi$_{0.8}$Co$_{0.15}$Al$_{0.05}$O$_2$, NCA) positive electrode material is responsible for the energy storage capability of the Panasonic's cylindrical 18650 cells. At present, only 65% of

lithium in LiNi$_{0.8}$Co$_{0.15}$Al$_{0.05}$O$_2$ (NCA) is reversibly removed and re-inserted in practice for energy storage, which is still far away from the theoretical limit (95% lithium removal).[3, 4] Bridging the gap between the practical and theoretical capacity of NCA would further increase the energy density of NCA-based batteries and the range of electric vehicles accordingly. More importantly, using NCA as a model compound to study the ultimate limits for reversible (de)intercalation can provide strategies that may help in the design of novel materials with improved electrochemical properties.

To extract all the electrochemically available lithium from an NCA electrode electrochemically, the cell should be charged to 4.8 V (vs. Li) or higher voltages, however, NCA shows fast capacity degradation when it is cycled with such a high cut-off charge voltage.[5] Several degradation mechanisms have been put forward from previous studies on the high voltage cycling of NCA.[6] The transmission electron microscopy (TEM) studies by Hwang et al. observed the structural transition from the layered structure (space group R$\bar{3}$m) to the disordered spinel structure (Fd$\bar{3}$m) and eventually to the rock-salt (Fm$\bar{3}$m) structure within a few atomic layers from the surface of overcharged NCA (with a nominal composition Li$_{0.1}$Ni$_{0.8}$Co$_{0.15}$Al$_{0.05}$O$_2$).[7, 8] These surface phases with spinel and/or rock salt structure are electrochemically inactive. *In-situ* X-ray diffraction (XRD) studies on the bulk structural changes of NCA charged to 4.9 V by Robert et al. found that, on charge, the c

a. Department of NanoEngineering, University of California San Diego, 9500 Gilman Drive, La Jolla, California 92093, USA *Email - shirleymeng@ucsd.edu, shirleymeng@gmail.com
b. X-ray Science Division, Advanced Photon Source, Argonne National Laboratory, Argonne, Illinois 60439, USA
c. Department of Chemistry, University of Cambridge, Lensfield Road, Cambridge, CB2 1EW, UK
d. Institute for Materials Research, SUNY Binghamton, Binghamton, New York 13902-6000, USA
e. Chemical and Engineering Materials Division, Oak Ridge National Laboratory, Oak Ridge, Tennessee 37830, USA
f. Advanced Li-ion Battery Engineering Laboratory and Key Laboratory of Graphene Technologies and Applications of Zhejiang Province, Ningbo Institute of Materials Technology & Engineering (NIMTE), Chinese Academy of Sciences, Ningbo, Zhejiang 315201, P. R. China

lattice experienced an initial expansion followed by a large contraction and 11% lithium remained in the structure at the end of charge at 4.9V.[5, 9] Morphological investigations by Sasaki et al. showed that primary NCA particles cracked and broke into tiny fragments, which were electrochemically disconnected and hence became non-active.[10] However, these studies have not demonstrated how the structure and atomic arrangements of the bulk change following high voltage cycling conditions.

Rietveld analysis of powder diffraction data is widely used to evaluate the atomic structure of crystalline phases.[11] Analysis of both X-ray and neutron scattering can provide complementary structural information because of different scattering mechanisms of neutrons and X-rays. By combining both X-ray and neutron scattering data, the most reliable structural models can be refined. Very bright synchrotron X-ray sources provide ready access to X-ray diffraction data, but given that the X-ray scattering power scales with the number of electrons, it can be difficult to distinguish elements of similar Z, or light elements (e.g. Li) in the presence of heavier elements. Neutron scattering contrast varies irregularly for different isotopes and elements, offering enhanced sensitivity to the light elements such as Li and O, and exhibits large scattering contrast between elements of similar Z in the periodic table.[12-14] However, the lower available flux of neutrons (compared to X-rays) can pose challenge for measurements on cycled electrode materials, as very large samples, typically gram-scale, are needed to obtain data with adequate signal-to-noise ratios. The combination of X-ray scattering and neutron scattering would enable a reliable and detailed crystal structural characterization.

To gain insight into the structural evolution changes that occur in NCA following cycling to high voltage, a series of samples were recovered from NCA||MCMB (MesoCarbon MicroBeads) batteries cycled to different states of charge, and the atomic bulk structure of the cycled positive electrode materials were probed using both synchrotron X-ray and neutron powder diffraction. The refinement results show an increased positional disorder of the transition metal atoms along the c axis, i.e. the layer stacking direction, with increasing cut-off voltage and an increase in the Li-Ni mixing only after the first cycle. The quantitative analyses of Li in NCA were carried out by both diffraction and ^{7}Li NMR, and the local structure of NCA was further characterized by magnetic measurements; the results corroborate well with the powder diffraction data.

Experimental details

Material

LiNi$_{0.8}$Co$_{0.15}$Al$_{0.05}$O$_2$ (NCA) positive electrode material was purchased from Toda American (NAT-1050). Inductively coupled plasma atomic emission spectroscopy (ICP-AES) was used to evaluate the composition of the metal species within the NCA positive electrode material. The measured composition was then used as initial parameters for the neutron diffraction Rietveld refinement.

Cell Assembly

Due to large samples required for neutron scattering measurements, ~ 1.6 g of NCA was used to perform the diffraction measurement. To prepare a large amount of sample for characterization, custom pouch cells were designed and assembled in a dry room at NIMTE's (Ningbo Institute of Materials Technology & Engineering) fabrication facility. The cell included 10 pieces of dual sided anode (MCMB) and NCA positive electrode. The positive electrode was composed of 92% NCA, 5% super P, and 3% PVDF on an aluminum current collector. The anode was composed of 91% MCMB, 4% super P, 2% CMC, and 3% SBR (Styrene-Butadiene Rubber) on a copper current collector. A Celgard separator was used to alternatively cover the anode and cathode on each side. The electrolyte solution composed of 1 M LiPF$_6$ in a 3:7 (volume fraction) ethylene carbonate (EC):dimethyl carbonate (DMC).

Neutron and X-ray Diffraction Analysis

The cycled samples were recovered by disassembling cycled pouch cells in an argon-filled glovebox. The positive electrode was washed with DMC 3 times and then allowed to dry in an argon atmosphere overnight. The NCA powder was scraped off from the positive electrode and was subsequently loaded into vanadium cans and polyimide (Kapton) tubes for neutron and X-ray scattering, respectively. These samples were well sealed in the glovebox to avoid air contamination. Time-of-fight (TOF) powder neutron diffraction data were collected at the VULCAN instrument at Spallation Neutron Sources (SNS) Oak Ridge National Laboratory (ORNL).[15] Approximately 1.6 g of powder was filled into a vanadium sample can. An incident beam (5mm×12mm) of 0.7 to 3.5 Å bandwidth, allowing 0.5~2.5 Å d-space in the diffracted pattern of the ±90° 2θ detector banks, was selected using the double-disk choppers at 30 Hz frequency. High-resolution mode was employed with Δd/d ~0.25%. The SNS was at nominal, 1100kW, power.[15] Each neutron diffraction pattern was collected for 3 h and reduced using VDRIVE software.[16] High energy synchrotron X-ray powder diffraction was taken at beamline 11-ID-B (λ= 0.2114 Å) at the Advanced Photon Source (APS) at Argonne National Laboratory (ANL). Two-dimensional images were collected at a nominal sample-to-detector distance of 95 cm using an amorphous Silicon area detector and reduced to 1 dimensional diffraction patterns within fit2d.[17] Variable temperature measurements were undertaken for NCA recovered following charge to 4.7 V in the temperature range 100-400 K using an open flow N$_2$ Oxford Cryostream 700 plus for temperature control. Rietveld refinement of the neutron and X-ray diffractions was performed simultaneously using GSAS software with EXPGUI interface.[18, 19]

Solid state NMR measurement

^{7}Li magic angle spinning (MAS) NMR spectra were acquired on a Bruker Avance II (4.7 T) magnetic using a 1.3mm MAS probe. The spectra were referenced to solid Li$_2$CO$_3$ at 0 ppm using a 90° (π/2) pulse of 1.08 µs at a power of 43.5 W. All spectra were acquired with a rotor-synchronised Hahn-echo sequence with a recycle delay of 0.1 s. The ^{7}Li spectra were processed and integrated in the Topspin software (version 3.0), in which the baseline of each spectrum was corrected with a polynomial function.

Magnetic measurement

Magnetic measurements were taken using a Quantum Design SQUID magnetometer (MPMS XL-5). The pristine NCA powder as well as the cycled samples collected from the pouch cells were sealed in plastic capsules in Ar-filled glovebox to avoid exposure to air. Temperature dependences of the magnetization were measured cooling the samples from 350 K to 2 K in a magnetic field of 1000 Oe. To measure zero-field-cooled (ZFC) temperature dependences of the magnetization, the remnant magnetic field was first quenched to less than 3 mOe, the sample was cooled to 2 K, then the field of 10 Oe was set and the temperature dependence of the magnetization was measured heating the sample to 300 K. Field-cooled (FC) dependences were measured upon cooling the sample in the same field of 10 Oe. Before taking magnetization curves, the sample was zero-field cooled to 2 K as described above. The magnetization was measured in the fields up to 5 T.

Results and Discussions

Neutron and X-ray Diffraction

The pristine NCA powder shows agglomerated, spherical secondary particles of less than 10 μm diameter, and the size of primary particle ranges from 300 nm to 1 μm (See Figure S1 a and b). Figure S1 c) represents the neutron diffraction data and Rietveld refinement results of the pristine NCA powders. All diffraction peaks of NCA material can be indexed to the hexagonal structure with $R\bar{3}m$ space group.[20, 21] There are only 1.0(2) % Ni distributed in the Li layer of pristine NCA, which indicates that the Toda NCA is well prepared with high quality.

The NCA assembled in a pouch cell delivers a charge capacity of 264 mAh g^{-1} and a discharge capacity of 210 mAh g^{-1} in its first cycle. The discharge capacity drops to 196 mAh g^{-1} after two cycles. In order to study the cycling stability of NCA within different voltage windows, the charge and discharge current are increased to 100 mA g^{-1} (C/2). When the voltage window is narrowed to 2.8 - 4.2V (low voltage), the NCA delivers a lower initial discharge capacity of 163 mAh g^{-1}. After 70 cycles, it still maintains a capacity of 161 mAh g^{-1}, which results in a high capacity retention of 98.8%. In contrast, the initial discharge capacity of NCA cycled between 2.8 - 4.7V (high voltage) increased to 200 mA g^{-1}, but degraded rapidly to 159 mA g^{-1} after 70 cycles. Besides the large capacity fade of 41 mAh g^{-1}, a large polarization of ~0.3 V is also observed, which indicates increased impedance with high voltage cycling. For detailed electrochemical results, please see Figure S2.

All NCA samples (from pouch cells) characterized here are either highly delithiated NCA in the initial cycles, or in the discharged states after a number of charge-discharge cycles. Rietveld refinement was employed to analyze the neutron and X-ray diffraction data simultaneously. Figure S3 shows the neutron diffraction patterns of NCA at different states of (dis)charge during the first cycle. With increased state of delithiation, all the

diffraction peaks become broadened. The peak broadening in diffraction patterns could be attributed to the particle size reducing and/ or the local strain.[22] Since the average NCA particle size does not change during the first few cycles, the peak broadening was refined using Stephens' strain-broadening model.[14, 23] Figure 1 demonstrates the joint X-ray and neutron diffraction refinement profile of NCA at 4.7V on the first charge. Based on the charge capacity, there is only 0.057 Li remaining within the NCA, indicating that all the electrochemically accessible Li has been extracted (based on the assumption that Al is not redox active). The irreversible formation of the O1 phase has been reported in many cases, when layered oxides are almost completely delithiated. Robert et al. reported the appearance of the O1 phase at 4.9V,[5] while Yin et al. observed the O1 phase after 0.74 lithium is extracted from LiCo$_{1/3}$Ni$_{1/3}$Mn$_{1/3}$O$_2$ (NMC) via XRD.[24] In the present study, Li$_{0.057}$Ni$_{0.8}$Co$_{0.15}$Al$_{0.05}$O$_2$ (NCA charged to 4.7V) can be well modeled by an O3 phase ($R\bar{3}m$), however, the observed patterns show appreciable differences with the calculated patterns, which assume isotropic atomic displacement parameters for all atoms, for diffraction peaks arising from crystal planes oriented parallel to or forming small angles with the (00l) planes . Refinement of the anisotropic atomic displacement parameters (ADPs) for atoms occupying the transition metal layer substantially improves the fitting and leads to a significantly reduced R factors. (Figure 1 b) and d)) The implications of anisotropic ADPs are further discussed later in the section. Therefore, all joint refinements in this work are carried out with anisotropic ADP. The refined profiles and detailed structure information are presented in the supplemental information (Fig S5 - 13, Table S2-10).

Figure 2 a) shows the evolution of the lattice parameters of NCA at different states of (dis)charges. During charge, Li is extracted from the layered structure while Ni^{3+} and Co^{3+} are oxidized to Ni^{4+} and Co^{4+}, with reduced ionic radii (e.g., r Ni^{3+} = 0.60 Å, r Ni^{4+} = 0.48 Å). The decrease in the ionic radii upon oxidation thus contributes to a contraction of the *a* lattice parameter by 1.95% from (2.86466(4) to 2.80885(4) Å).[12, 13] As lithium is inserted back to NCA during discharge, the *a* lattice parameter increased to 2.85742(2) Å as a result of transition metal ion reduction, but is still 0.25% smaller than that at the pristine state. This irreversible decrease of a lattice parameter indicates the oxidized transition metal ions were not completely reduced, and there was 11.7(8)% lithium, based on the refinement result, that did not intercalate back to NCA. Figure S4 shows the bond length between the transition metal and oxygen (TM-O), which is another indicator of the transition metal oxidation state, because the oxidation of TM ions increased the electrostatic attraction between the TM ions and oxygen ions and decreased the bond length of TM-O. At the end of the first cycle, the TM-O bond does not restore to the value at the pristine state, again suggesting the structure is not fully lithiated. At early stages of charge, the removal of lithium introduces an electrostatic repulsion from adjacent oxygen layers, accounting for the initial increase of the *c* lattice parameter.[24, 25] However, the NCA at 4.3V already displays *a* smaller *c* lattice parameter than in the pristine state. The *c* lattice contraction in the highly delithiated state is due to the increased covalency of the TM-O bond, which plays a significant role in decreasing the electrostatic repulsion from adjacent oxygen

layers.[25] On further delithiation, the c lattice parameter collapses to 13.8216(4) Å, which is 2.55% smaller than at the pristine state. After the first discharge, the c lattice becomes 0.19% larger than at the pristine state. The changes in the a and c lattice parameters during the second cycle are consistent with the observation during the first charge. After 70 cycles, the NCA cycled to a higher cut-off voltage (4.7V) exhibits a higher degree of irreversible a, c lattice parameter change than the NCA cycled to a lower cut-off voltage. This irreversible lattice change is caused by the loss of the lithium during electrochemical cycling.

The Ni content in the lithium layer is only 1.0(2) % in the pristine state. In the Ni based layered oxides, as the lithium is extracted during the charge, some of the Ni in the TM layer migrates to the lithium layer.[3, 26] At 4.3V, the Ni content in the lithium layer increases slightly to 1.6(1) %. As shown in Figure 2 b), the Ni migration ceases after 4.3V on first charge. Even after 70 cycles, the Ni concentration in the lithium layer remains at a relatively constant amount of 2%. Since neutrons are sensitive to the presence of lithium, the lithium content of NCA has also been investigated in this study. The 1.0(2) % lithium in the TM layer has already migrated to the lithium layer at charge states no later than 4.3V. There is no lithium inserted back to the TM layer upon the following cycles. The refined lithium content is compared with the value calculated from the capacity in Figure 2 c). At voltages above 4.3V during the first charge, more lithium was consumed in the overall electrochemical reaction than was actually extracted from the bulk NCA (Figure 2c). At 4.7V, 0.097(12) lithium per formula unit of NCA remained in the crystal structure., which shows that at least 95% of the electrochemically available lithium can be extracted.

The discrepancy between the calculated and refined lithium content at the end of first charge implies the presence of parasitic reactions, for example, oxidative electrolyte decomposition, no later than 4.3V during the first charge. At the end of the first cycle, the lithium content is 0.883(8), corresponding to a 12% loss of lithium in the bulk NCA. This incomplete intercalation of lithium explains the irreversible changes of the a and c lattice parameters. Since all the electrochemical tests are conducted in a pouch cell using the MCMB anode, this irreversible loss of lithium could come from the depletion of lithium on the anode side to form a stable solid electrolyte interphase (SEI).[27] In addition, Kasnatscheew's work showed the lithiation process is kinetically more impeded than the delithiation process in classical layered oxides, 61% of the irreversible lithium loss could be recovered after a constant potential step at a discharge cut-off potential, which confirmed this irreversible capacity is partially from the kinetic limitations.[27, 28]

At 4.7V on the second cycle, the lower lithium content calculated from the electrochemical capacity than from the refinement indicates that the oxidative electrolyte decomposition continues to occur in the high voltage region. The existence of the parasitic reactions consumes the electrolyte gradually and contributes to the irreversible capacity loss. As a result of an accumulation of 70 cycles, there is a big discrepancy between the calculated lithium occupancy and the refined lithium occupancy in the NCA sample that underwent high voltage (4.7V) cycling. The lithium content estimated from charge and discharge capacities from each cycle is only 0.56, while the refined lithium occupancy is 0.79(1). The NCA cycled within the high voltage range (2.8-4.7V) shows little lithium loss and maintains a well-layered structure without a phase transition in the bulk. In contrast, the NCA cycled within the low voltage range (2.8-4.2 V) contains only 0.814(9) lithium after 70 cycles. The systematic investigation on the bulk structure of NCA proves that the huge capacity degradation in Figure S2 c) is not due to the changes in the bulk structure. In previous work, Qian coated the surface of NCA with the lithium lanthanum titanate (LLTO) fast lithium-ion conductor, which prevents the NCA materials from being direct exposed to the electrolyte. The resulting capacity retention of LLTO coated NCA was much more enhanced than the uncoated one.[29] More efforts should be focused on engineering a better cathode/electrolyte interphase to realize the high voltage application of NCA. [30-33]

The evolution of the atomic displacement parameters (ADPs) reflects a progressive increase in the disorder of the transition metal species perpendicular to the layers at high voltage (Figure 3). $U_{11}(= U_{22})$, is an element of the ADP tensor that reflects disorder in the ab-plane, while U_{33} reflects disorder along the c direction.[34] In pristine NCA, U_{11} and U_{33} are of similar magnitudes indicating effectively isotropic ADPs. As Li is extracted, the ADPs become increasingly anisotropic. At 4.3V, U_{33} is more than 4 times larger than U_{11}, indicating a substantial disorder of the TM positions perpendicular to the c-axis. As additional Li is extracted, U_{33} continues to increase and, at 4.7V, is 10 times larger than U_{11}. This anisotropy decreases during discharge as Li is inserted, reaching a ratio of 1.5:1 (U_{33}:U_{11}) after the first cycle. This increase in anisotropy is also evident in the second charge. Similar studies have been conducted on the other two representative layered oxides, the Figure S14 demonstrates atomic displacement parameters of $LiNi_{0.5}Mn_{0.3}Co_{0.2}O_2$, and $LiNi_{1/3}Mn_{1/3}Co_{1/3}O_2$. These results confirm that the anisotropic disorder phenomena at highly charged states of layered oxides are not confined to NCA.

Both static and thermal displacement of the transition metal species can contribute to the large anisotropic ADPs found here (Figure 4). Static displacement is induced by displacement of individual atoms from their average crystallographic positions.[35] Thermal displacement, a function of temperature, reflects the thermal motion of atoms. To distinguish the static and thermal (i.e. the thermal motion of atoms) contributions to the anisotropic ADPs observed at high potentials, XRD data was collected for highly charged NCA (at 4.7V) as a function of temperature (100 K to 400K). At low temperatures, where the dynamic contribution to the disorder is effectively eliminated, the value of U_{33} was found to be much larger than that of U_{11}, demonstrating the static nature of the anisotropic disorder along the c-axis in this system.

^{7}Li NMR

The change in the local Li environments during cycling was further studied by solid-state ^{7}Li NMR as shown in Figure 5a). The variation in the total Li intensity is shown in Figure 5 b). As discussed in previous studies[36-38], the ^{7}Li NMR spectrum of pristine NCA can be

rationalized based on the distribution of Ni^{3+}, Co^{3+}, and Al^{3+} ions in the nearest neighbor (nn) and next nearest neighbor (nnn) configuration to Li ions within the $LiNi_{0.8}Co_{0.15}Al_{0.05}O_2$ structure. The dominant mechanism that leads to an observed shift is due to the Fermi contact interaction involving the unpaired electrons on the Ni^{3+} ions. The unpaired spin is transferred via an intervening O ion, which leads to 90 ° (nn) and 180 ° (nnn) Li-O-Ni bond pathways. Low spin Ni^{3+} $(t_{2g}^6 e_g^{*1})$ in NCA[36] and $LiNiO_2$[39] is known to undergo a positive Jahn-Teller (JT) distortion in which two of the Ni-O bonds in each NiO_6 octahedra are lengthened and four are shortened. At room temperature, thermal vibrations lead to a dynamic JT process in which the distortion on each Ni^{3+} center fluctuates. From previous computational and experimental studies[40, 41], it has been shown that the contribution to the total ^7Li shift of the 90 ° and 180 ° Li-O-Ni bond pathways are approximately −15 and 110 ppm, respectively, for a Ni^{3+} ion undergoing a dynamic Jahn-Teller distortion.

On delithiation to 4.3 V, the ^7Li resonances move to lower frequency and the spectrum contains one main peak at 32 ppm with a sharp, low intensity peak at -4 ppm. On further delithiation to 4.7 V, the spectrum contains a single peak at −1 ppm. As can be seen from Figure 5 b), the total Li contents predicted by NMR of 0.21 (4.3 V) and 0.13 (4.7 V) are slightly higher than those predicted by diffraction of 0.166 and 0.097, respectively. The changes in the Li shifts on delithiation are related to the changes in the oxidation states of the transition metal ions. Oxidation of Ni^{3+} $(t_{2g}^6 e_g^{*1})$ to Ni^{4+} $(t_{2g}^6 e_g^{*0})$ leads to a decrease in the number of unpaired electrons, as low spin Ni^{4+} is diamagnetic, which subsequently leads to a decrease in the number of nn and nnn Li-O-Ni^{3+} bond pathway contributions. Oxidation of diamagnetic Co^{3+} $(t_{2g}^6 e_g^{*0})$ to Co^{4+} $(t_{2g}^5 e_g^{*0})$ leads to an increase in the number of unpaired electrons. The Li-O-Co^{4+} bond pathway contributions have not been previously reported and it has been suggested in previous literature that the presence of localized holes on the Co^{3+} (i.e., paramagnetic Co^{4+} ions) should lead to a loss of signal intensity due to very fast relaxation.[42]

At a Li composition of 0.21 (4.3 V), if Ni was the only species to be oxidized with Co maintaining the Co^{3+} oxidation state, almost all (98.8 %) of the Ni ions should be in the Ni^{4+} oxidation state, which would result in a single diamagnetic environment with a peak at ~0 ppm. The peak at 32 ppm in the 4.3 V spectrum suggests that $Ni^{3+} \rightarrow Ni^{4+}$ and $Co^{3+} \rightarrow Co^{4+}$ oxidation occurs, which is consistent with a previous study on $LiNi_{0.3}Co_{0.7}O_2$.[40] Although paramagnetic Co^{4+} ions are expected to be present in the sample, a significant decrease in the ^7Li intensity was not observed at 4.3 V, which suggests that some Li sites with Co^{4+} neighbors are being directly observed, and contribute to the broad peak at 32 ppm. The Fermi contact shift contribution of localized Co^{4+} ions on the ^7Li NMR shift will be the focus of future work, but based on the shifts observed for Mn^{4+} ions $(t_{2g}^3 e_g^{*0})$, the positive shift is consistent with the shift expected for Li ions with nn Co^{4+} ions.

The peaks at -4 ppm (4.3 V) and -1 ppm (4.7 V) are largely related to diamagnetic Li environments as a result of Ni^{4+} and Al^{3+} species within the nn and nnn positions of the NCA structure. Part of the Li intensity near 0 ppm may also be due to diamagnetic surface

phases or residual electrolyte, which may account for the slight increase in the Li content calculated with NMR compared to diffraction.

Upon first discharge to 2 V, the Li distribution shifts back to higher frequency as the Ni^{4+} and Co^{4+} ions are reduced to Ni^{3+} and Co^{3+}. The Li content at the end of first discharge is 0.85, which is consistent with the refined Li content from diffraction of 0.883. After 70 cycles, the Li content predicted from NMR for the samples cycled in the low and high voltage ranges is reduced to 0.80 and 0.71, respectively, again suggesting that less Li returns to the structure, particularly after cycling in the high voltage regime. The overall distribution decreases in shift as the Li content in $Li_xNi_{0.8}Co_{0.15}Al_{0.05}O_2$ is reduced from pristine (x = 1), to x = 0.85 after the 1st cycle following discharge to 2V and further to x = 0.8 (70 cycles low) and x = 0.71 (70 cycles high). In a previous study,[37] it was suggested that the variation in the ^7Li NMR shift in NCA to lower frequencies after multiple cycles (120 cycles) was primarily related to the migration of Ni ions and to a lesser extent due to the oxidation state of Ni. Using the nearest neighbor and next nearest neighbor pathway contributions of -15 and 110 ppm for Ni^{3+}, assuming a random distribution of $Ni^{3+/4+}$, Co^{3+}, and Al^{3+} sites and that only $Ni^{3+} \rightarrow Ni^{4+}$ oxidation occurs, the expected ^7Li shift distributions from the different discharged samples were modeled as shown in Figure S15.

As it can be seen from Figure S15, the variation in the ^7Li NMR shift in the current work is well described by the changes in the Ni oxidation state as a result of the differences in the Li content. However, there may also be a small contribution to the ^7Li NMR shift from Ni migration as the amount of Ni in the Li layer is predicted from diffraction to be 1.5 and 2.1 % for the low and high voltage range cycled samples, respectively.

Magnetic Analysis

Magnetic susceptibility of NCA follows the Curie-Weiss law down to 50 K as indicated by the linear temperature dependence of the reciprocal susceptibility (Figure 6). The effective magnetic moment normalized per mole of transition metals (TM) is 1.98 μ_B (Table S11), which is a bit higher than the spin-only value for Ni^{3+} due to the orbital contribution, consistent with the values observed for $LiNiO_2$.[43] The magnetization curve shows very small hysteresis with a remnant magnetization of about 0.001 μ_B (Figure 7 a)). The FC-ZFC curves (Figure 7 b)) show a cusp at T_f=6.5 K typical of a spin-glass transition. A similar transition is observed in the most stoichiometric samples of $Li_{1-x}Ni_{1+x}O_2$ (x≈0.004) at 7.5 K.[44] Less stoichiometric samples of $Li_{1-x}Ni_{1+x}O_2$ show FC and ZFC curves departing at higher temperatures, for example at x≈0.02 FC and ZFC curves start to depart at 240 K.[45] Thus, FC-ZFC curves can be used as an indicator of the amount of Ni in the Li layer. Such Ni_{Li} ions form ferrimagnetic clusters due to a strong magnetic exchange with Ni ions in the TM layer, so that T_f depends both on the amount of Ni/Li exchange and on the nature of TM ions in the TM layer. NCA has 0.2 of zero-spin Co^{3+} and Al^{3+} ions in the transition metal layer, thus it is expected to show lower T_f per similar amount of Ni_{Li} as compared to $LiNiO_2$. Therefore, $T_f \approx 6.5$ K indicates a very small amount of Li/Ni exchange consistent with 1% found by structural refinement.

ARTICLE

Upon charge to 4.3 V, the effective magnetic moment decreases as expected upon oxidation of Ni^{3+} (S=1/2) to Ni^{4+} (S=0). On the other hand, upon Co^{3+} (S= 0) to Co^{4+} (S=1/2) oxidation, the magnetic moment increases, which is observed upon further charge to 4.5 and 4.7 V (Figure 6, Table S11). The experimentally observed effective magnetic moments are fairly close to the ones calculated assuming Li contents from the Rietveld refinement, spin-only magnetism and oxidation of all Ni^{3+} to Ni^{4+} followed by oxidation of Co^{3+} ions. Due to the small amount of magnetic ions in the charged samples, it is hard to tell from the magnetization data whether Co^{3+} is being oxidized simultaneously with Ni^{4+} at these voltages.

The reciprocal temperature dependence of the magnetic susceptibility of discharged samples in comparison with those of pristine NCA is summarized in Figure 6. The higher slope of the dependence after cycling indicates a lower magnetic moment than in the pristine sample, which is a result of incomplete Ni^{4+} reduction. It is interesting to note that the biggest difference is observed after the first cycle, while the subsequent cycling up to 70 cycles results in smaller changes in the effective magnetic moment of the discharged samples. The cycling with the higher voltage cut-off leads to a slightly lower effective magnetic moment than the cycling in the smaller voltage window, indicating that less Li has returned into the structure in the former case. Comparison between the experimentally observed effective moments and those calculated using Li contents from the Rietveld refinements indicates that the two sets follow the same trend. As in the case of pristine NCA, the higher values of the experimental magnetic moment reflect the orbital contribution of typical of Ni^{3+} ions.

The evolution of Li/Ni exchange upon cycling can be followed by comparing the magnetization curves and FC/ZFC susceptibilities of the discharged samples. Figure 7 indicates that the hysteresis loop slightly increases after the first cycle, however, the subsequent cycling does not lead to a further increase. A similar trend is observed in the FC/ZFC curve; after the first cycle FC and ZFC curves start to depart at much higher temperature than in the pristine sample, around 100 K. After the second cycle, the difference between FC and ZFC curves increases, but further cycling does not lead to noticeable changes. The cusp typical of the spin-glass transition is observed in all the discharged samples at 6.5 K. This data indicates that the amount of Ni/Li exchange increases after the first cycle and does not undergo significant changes upon further cycling, consistent with the Rietveld refinement results.

Conclusions

Joint X-ray and neutron scattering, ^{7}Li NMR, and magnetic studies on NCA material were performed on *ex situ* powder samples from a custom 1 Ah pouch full cell with MCMB anode. NCA maintains the O3 structure up to 95% extraction of the electrochemically available lithium. The Ni migration to the Li layer is only observed during the first charge. The quantification of lithium content in NCA shows that the capacity degradation at high voltages comes from the parasitic oxidation of the electrolyte instead of the bulk structure degradation. Anisotropic ADPs were observed and quantified. It is demonstrated for the first time that the transition metal layer becomes more disordered along the *c*-axis than along the *a*- and *b*- axes at highly charged states. Further investigation indicates that this anisotropic disorder results from static disorder. These results provide new insights into the bulk crystal structure evolution of NCA layered oxides after extremely high voltage cycling and demonstrate that light elements in the bulk can be quantified via a combination of joint X-ray and neutron diffraction, ^{7}Li NMR, and magnetic measurements.

Conflicts of interest

There are no conflicts to declare.

Acknowledgements

NOTICE OF COPYRIGHT

Author Contributions

H.D.L., H.L., and Y.S.M. designed the experiment. H.D.L. tested the electrochemical performances and prepared all the ex-situ samples. H.D.L., S.H., M.Z., Y.C., and K.A. recorded ND

experiment data. H.L., K.M.W., O.J.B., S.H.L., P.J.C., and K.W.C. recorded XRD experiment data and data analyses. I.D.S., N.M.T., and C.P.G performed the NMR experiments and analyses. N.C., and M.S.W performed the magnetic experiments and analyses. B.Q., Y.X., and Z.L. prepared pouch cells. H.D.L. and H.L. conducted the ND and XRD joint analysis. Y.S.M. supervised the research. All authors contributed to the discussion and provided feedback on the manuscript.

Notes and references

1   1.   J. Cobb, Tesla Model S Crossed 100,000 Sales Milestone This Month, http://www.hybridcars.com/tesla-model-s-crossed-100000-sales-milestone-this-month/).

2   2.   https://www.teslamotors.com/about).

3   3.   M. S. Whittingham, *Chemical Reviews*, 2004, **104**, 4271-4301.

4   4.   M. S. Whittingham, *Chemical Reviews*, 2014, **114**, 11414-11443.

5   5.   R. Robertz and P. Novak, *J Electrochem Soc*, 2015, **162**, A1823-A1828.

6   6.   M. D. Radin, S. Hy, M. Sina, C. Fang, H. Liu, J. Vinckeviciute, M. Zhang, M. S. Whittingham, Y. S. Meng and A. Van der Ven, *Advanced Energy Materials*, DOI: 10.1002/aenm.201602888, 1602888-n/a.

7   7.   S. Hwang, W. Chang, S. M. Kim, D. Su, D. H. Kim, J. Y. Lee, K. Y. Chung and E. A. Stach, *Chem Mater*, 2014, **26**, 1084-1092.

8   8.   S. M. Bak, K. W. Nam, W. Chang, X. Q. Yu, E. Y. Hu, S. Hwang, E. A. Stach, K. B. Kim, K. Y. Chung and X. Q. Yang, *Chem Mater*, 2013, **25**, 337-351.

9   9.   R. Robert, C. Bunzli, E. J. Berg and P. Novak, *Chem Mater*, 2015, **27**, 526-536.

10   10.   T. Sasaki, V. Godbole, Y. Takeuchi, Y. Ukyo and P. Novak, *J Electrochem Soc*, 2011, **158**, A1214-A1219.

11   11.   B. Qiu, M. H. Zhang, L. J. Wu, J. Wang, Y. G. Xia, D. N. Qian, H. D. Liu, S. Hy, Y. Chen, K. An, Y. M. Zhu, Z. P. Liu and Y. S. Meng, *Nature Communications*, 2016, **7**.

12   12.   H. Liu, Y. Chen, S. Hy, K. An, S. Venkatachalam, D. Qian, M. Zhang and Y. S. Meng, *Advanced Energy Materials*, 2016, DOI: 10.1002/aenm.201502143, n/a-n/a.

13   13.   H. D. Liu, C. R. Fell, K. An, L. Cai and Y. S. Meng, *Journal of Power Sources*, 2013, **240**, 772-778.

14   14.   H. Liu, H. Liu, S. H. Lapidus, Y. S. Meng, P. J. Chupas and K. W. Chapman, *J Electrochem Soc*, 2017, **164**, A1802-A1811.

15   15.   K. An, H. D. Skorpenske, A. D. Stoica, D. Ma, X. L. Wang and E. Cakmak, *Metall Mater Trans A*, 2011, **42A**, 95-99.

16   16.   K. An, X. L. Wang and A. D. Stoica, *Journal*, 2012.

17   17.   A. P. Hammersley, S. O. Svensson, M. Hanfland, A. N. Fitch and D. Hausermann, *High Pressure Research*, 1996, **14**, 235-248.

18   18.   A. C. Larson and R. B. V. Dreele, *Los Alamos National Laboratory Report (LAUR)*, 2004, **86-748**.

19   19.   B. H. Toby, *J Appl Crystallogr*, 2001, **34**, 210-213.

20   20.   H. Liu, D. Qian, M. G. Verde, M. Zhang, L. Baggetto, K. An, Y. Chen, K. J. Carroll, D. Lau, M. Chi, G. M. Veith and Y. S. Meng, *Acs Applied Materials & Interfaces*, 2015, **7**, 19189-19200.

21   21.   M. G. Verde, H. D. Liu, K. J. Carroll, L. Baggetto, G. M. Veith and Y. S. Meng, *Acs Applied Materials & Interfaces*, 2014, **6**, 18868-18877.

22   22.   D. Balzar, *International Union of Crystallography Monographs on Crystallography*, 1999, **10**, 94-126.

23   23.   P. W. Stephens, *J Appl Crystallogr*, 1999, **32**, 281-289.

24   24.   S. C. Yin, Y. H. Rho, I. Swainson and L. F. Nazar, *Chem Mater*, 2006, **18**, 1901-1910.

25   25.   N. Yabuuchi, Y. Makimura and T. Ohzuku, *J Electrochem Soc*, 2007, **154**, A314-A321.

26   26.   S. Hy, H. Liu, M. Zhang, D. Qian, B.-J. Hwang and Y. S. Meng, *Energy & Environmental Science*, 2016, DOI: 10.1039/c5ee03573b.

27   27.   J. Kasnatscheew, M. Evertz, B. Streipert, R. Wagner, R. Klopsch, B. Vortmann, H. Hahn, S. Nowak, M. Amereller, A. C. Gentschev, P. Lamp and M. Winter, *Phys Chem Chem Phys*, 2016, **18**, 3956-3965.

28   28.   A. Grenier, H. Liu, K. M. Wiaderek, Z. W. Lebens-Higgins, O. J. Borkiewicz, L. F. J. Piper, P. J. Chupas and K. W. Chapman, *Chem Mater*, 2017, **29**, 7345-7352.

29   29.   D. N. Qian, B. Xu, H. M. Cho, T. Hatsukade, K. J. Carroll and Y. S. Meng, *Chem Mater*, 2012, **24**, 2744-2751.

30   30.   H. Liu, M. Wolf, K. Karki, Y.-S. Yu, E. A. Stach, J. Cabana, K. W. Chapman and P. J. Chupas, *Nano Letters*, 2017, **17**, 3452-3457.

31   31.   J. Huang, H. Liu, T. Hu, Y. S. Meng and J. Luo, *Journal of Power Sources*, 2018, **375**, 21-28.

32   32.   J. Huang, H. Liu, N. Zhou, K. An, Y. S. Meng and J. Luo, *Acs Applied Materials & Interfaces*, 2017, DOI: 10.1021/acsami.7b09903.

33   33.   H. D. Liu, J. J. Huang, D. N. Qian, S. Hy, C. C. Fang, J. Luo and Y. S. Meng, *J Electrochem Soc*, 2016, **163**, A971-A973.

34   34.   H. Wang, Y. Chen, Z. D. Hood, G. Sahu, A. S. Pandian, J. K. Keum, K. An and C. Liang, *Angewandte Chemie International Edition*, 2016, **55**, 8551-8555.

35   35.   Y. Chen, Y. Cheng, J. Li, M. Feygenson, W. T. Heller, C. Liang and K. An, *Advanced Energy Materials*, 2017, **7**, n/a-n/a.

36   36.   N. M. Trease, I. D. Seymour, M. D. Radin, H. Liu, H. Liu, S. Hy, N. Chernova, P. Parikh, A. Devaraj, K. M. Wiaderek, P. J. Chupas, K. W. Chapman, M. S. Whittingham, Y. S. Meng, A. Van der Van and C. P. Grey, *Chem Mater*, 2016, **28**, 8170-8180.

37   37.   F. Dogan, J. T. Vaughey, H. Iddir and B. Key, *Acs Applied Materials & Interfaces*, 2016, **8**, 16708-16717.

38   38.   N. Leifer, O. Srur-Lavi, I. Matlahov, B. Markovsky, D. Aurbach and G. Goobes, *Chem Mater*, 2016, **28**, 7594-7604.

39   39.   A. Rougier, C. Delmas and A. V. Chadwick, *Solid State Commun*, 1995, **94**, 123-127.

40   40.   D. Carlier, M. Menetrier and C. Delmas, *J Mater Chem*, 2001, **11**, 594-603.

41   41.   D. S. Middlemiss, A. J. Ilott, R. J. Clement, F. C. Strobridge and C. P. Grey, *Chem Mater*, 2013, **25**, 1723-1734.

42   42.   M. Menetrier, I. Saadoune, S. Levasseur and C. Delmas, *J Mater Chem*, 1999, **9**, 1135-1140.

43   43.   A. Rougier, P. Gravereau and C. Delmas, *J Electrochem Soc*, 1996, **143**, 1168-1175.

44   44.   E. Chappel, M. D. Nunez-Regueiro, S. de Brion, G. Chouteau, V. Bianchi, D. Caurant and N. Baffier, *Phys Rev B*, 2002, **66**.

45   45.   E. Chappel, M. D. Nunez-Regueiro, G. Chouteau, A. Sulpice and C. Delmas, *Solid State Commun*, 2001, **119**, 83-87.

46

Journal of Materials Chemistry A Accepted Manuscript

View Article Online

Please do not adjust margins
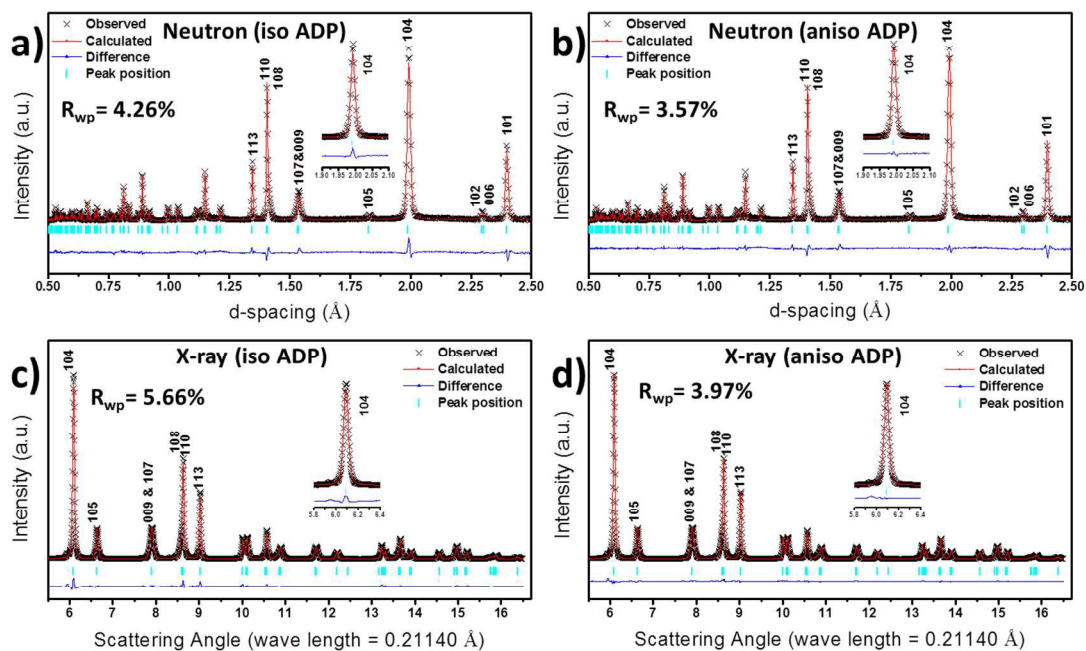
Figure 1. X-ray and Neutron diffraction data joint refinement of NCA at 4.7V on first charge. a) Neutron and c) X-ray refinement from isotropic atomic displacement parameters model, b) Neutron and d) X-ray refinement from anisotropic atomic displacement parameters model.
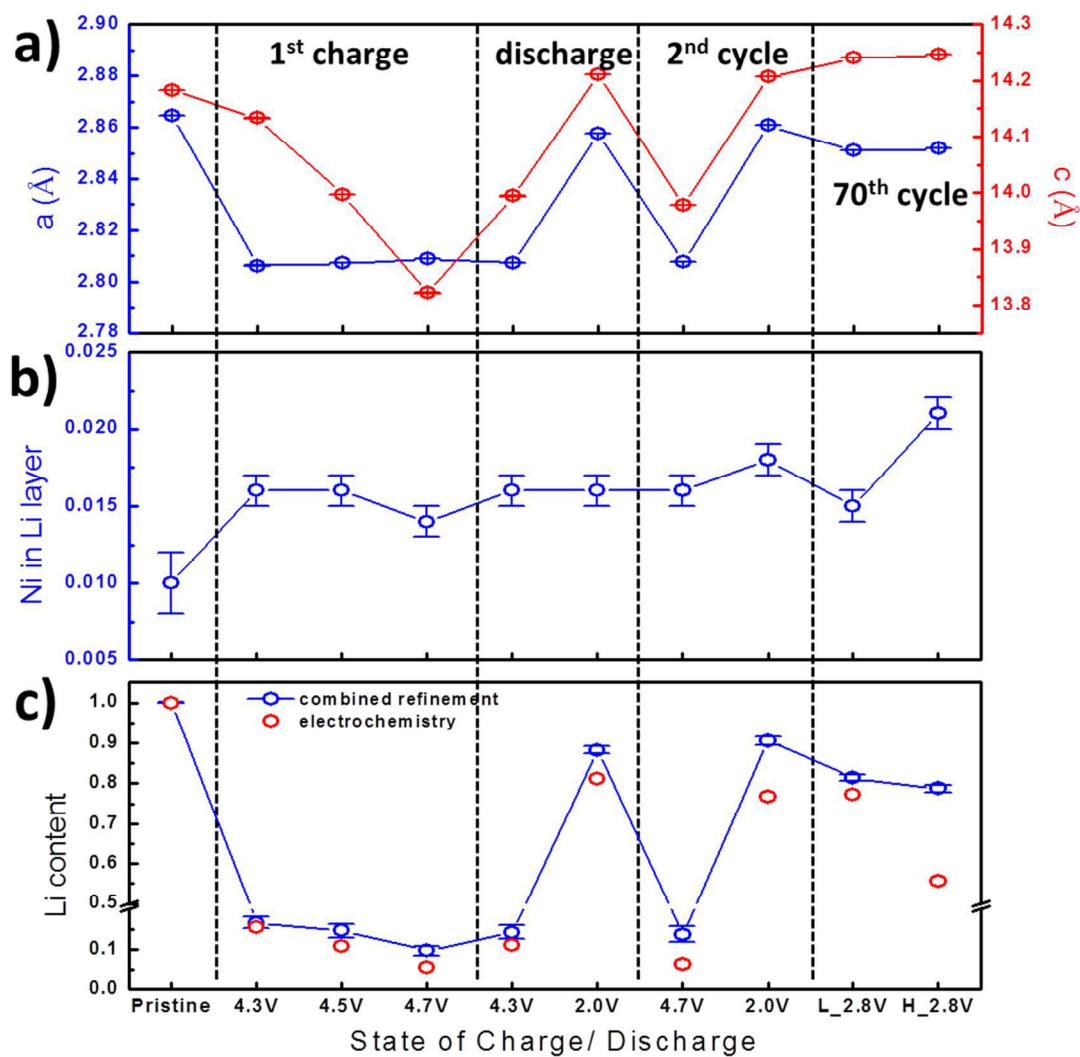
1

Figure 2. X-ray and Neutron diffraction data joint refinement results: a) Lattice parameters, b) Ni content in Li layer, and c) Li content at different states of (dis)charge.
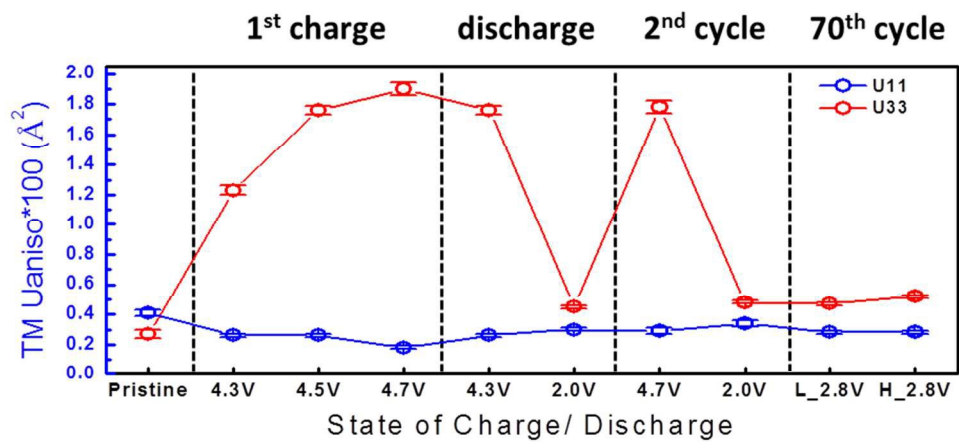
Figure 3. Atomic displacement parameters from X-ray and Neutron diffraction data joint refinement.

3
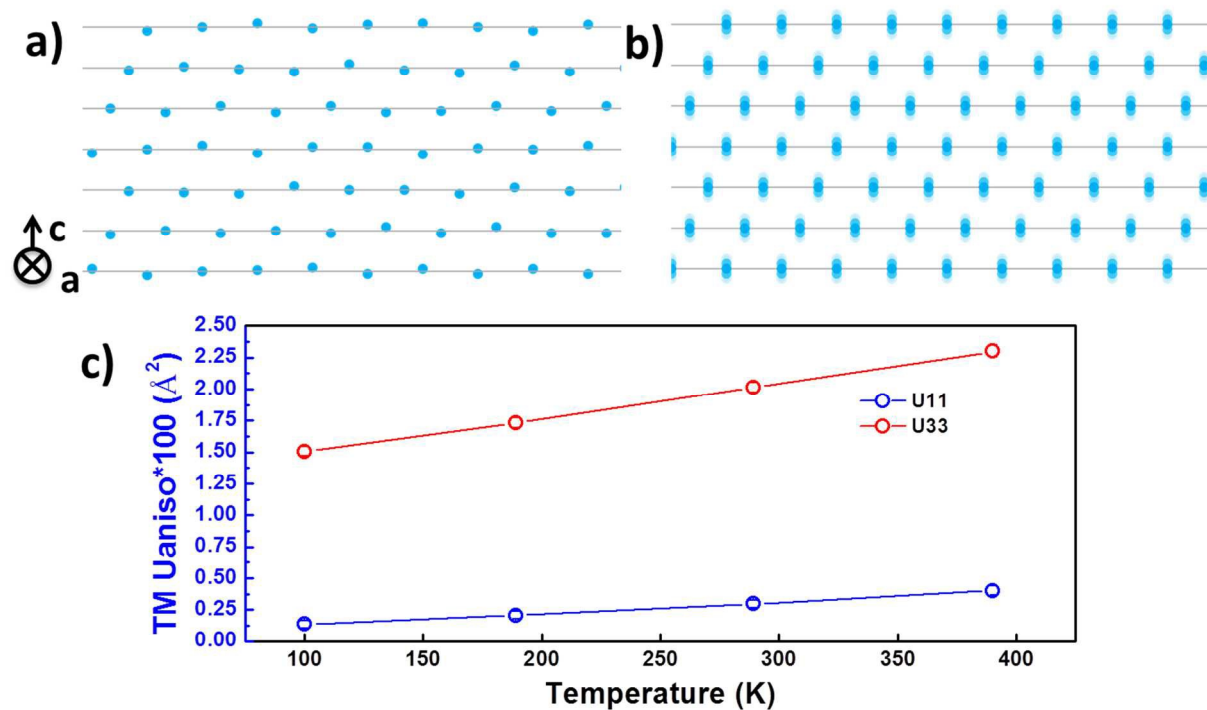
Figure 4. a) Schematic of static displacement; b) thermal displacement; c) Atomic displacement parameters at various temperatures from X-ray diffraction data. (NCA at 4.7V on the first charge)
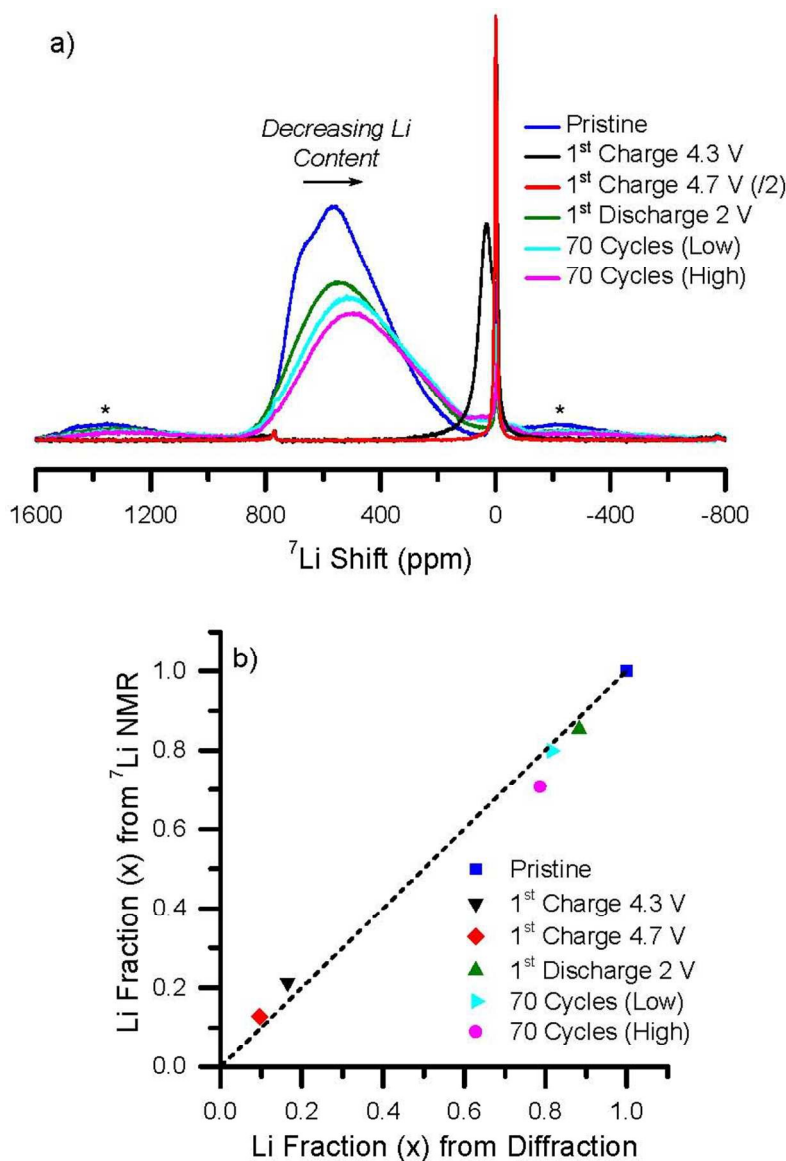
4

Figure 5. a) ^{7}Li MAS NMR spectra of $Li_xNi_{0.8}Co_{0.15}Al_{0.05}O_2$ (NCA) at different states of states of (dis)charge on the first cycle and after 70 cycles in the low (2.8—4.2 V) and high (2.8—4.7 V) voltage windows. Spectra were acquired at a spinning frequency of 60 kHz under an external magnetic field of 4.7 T. Asterisks (*) show the position of spinning sidebands. The intensity of the individual spectra has been scaled by the sample mass and the number of scans. The intensity of the sample at 4.7 V on the first charge has additionally been scaled down by a factor of two to aid comparison. b) Comparison of Li fraction (x) obtained from ^{7}Li NMR and combined X-ray/Neutron diffraction.
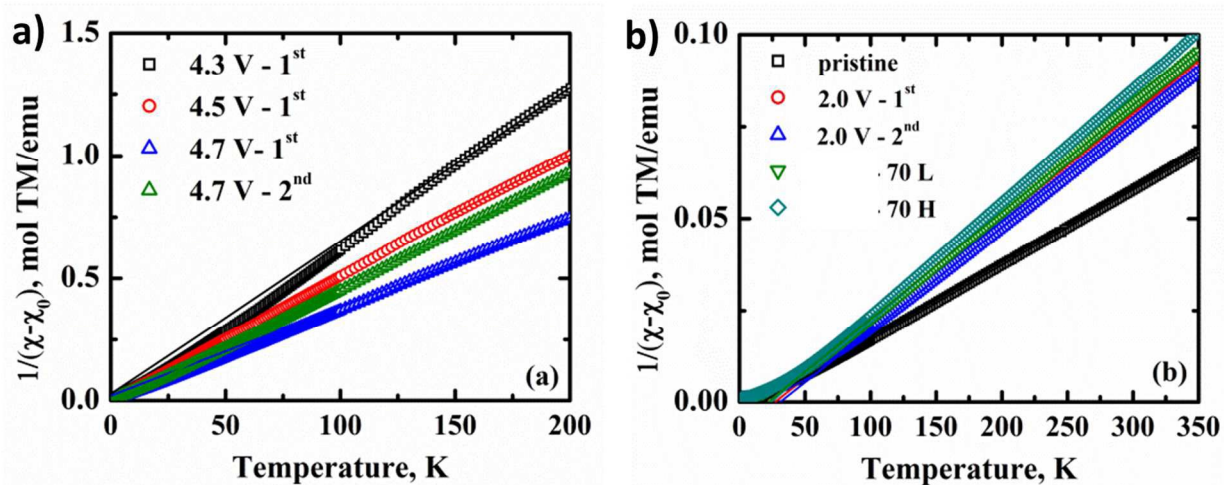
Figure 6. Reciprocal magnetic susceptibilities of a) charged and b) discharged NCA and their fit to the Curie-Weiss law. 4.3 V - 1st indicates the voltage and the cycle number. 70 L refers to cycling between 2.8 and 4.2 V and 70 H to cycling between 2.8 and 4.7 V.
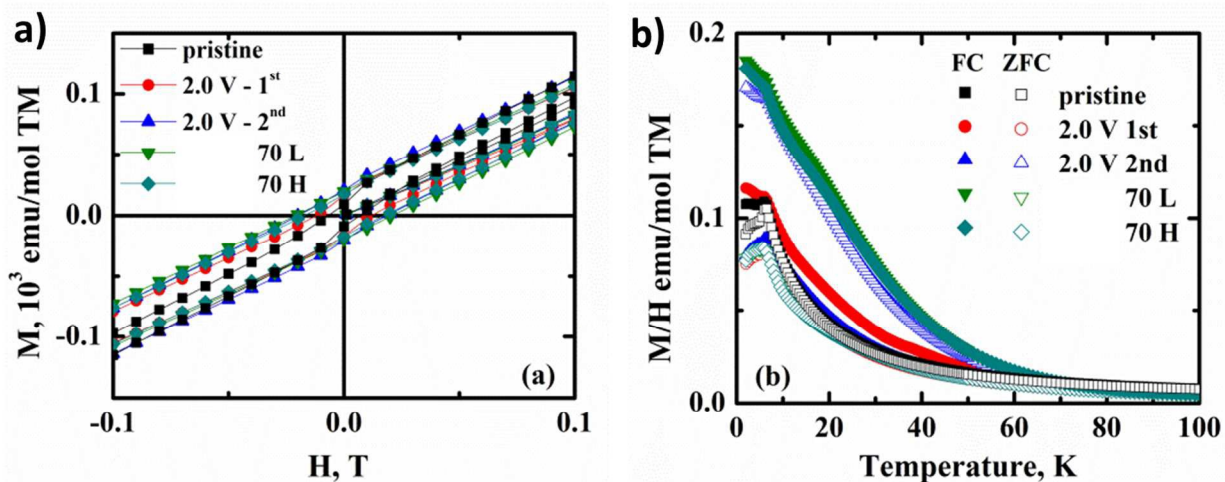
6

Figure 7 a) Magnetization at 2 K and (b) FC-ZFC curves of pristine and discharged NCA. 2.0 V - 1st indicates the discharge voltage and the cycle number. 70 L refers to cycling between 2.8 and 4.2 V and 70 H to cycling between 2.8 and 4.7 V.